buildings

MDPI

Article

Tensile-to-Shear Crack Transition in the Compression Failure of Steel-Fibre-Reinforced Concrete: Insights from Acoustic Emission Monitoring

Zihan Jiang, Zhiwen Zhu * and Federico Accornero

Department of Civil Engineering and Smart Cities, Shantou University, Shantou 515063, China; 19zhjiang@stu.edu.cn (Z.J.); federico@stu.edu.cn (F.A.)
* Correspondence: zhuzw@stu.edu.cn

Abstract: Steel-fibre-reinforced concrete (SFRC) has been increasingly used in the field of engineering structures in recent years. Hence, the accurate monitoring of the fracturing process of in-service SFRC has considerable significance in terms of structural safety. This paper investigates the acoustic emission (AE) and digital image correlation (DIC) features characterising the damage behaviour of SFRC samples in compression. For all the tests, cumulated AE, *b*-value, β_t coefficient, average frequency, and rise angle are considered to describe the actual SFRC failure mechanisms. The results show that SFRC exhibits enhanced toughness compared to normal concrete (NC), with an indicated transition from a brittle to a ductile structural behaviour. This improved behaviour can be attributed to the bridging effect of steel fibres, which also drives the progressive tensile-to-shear crack transition, thus being the main cause of the final SFRC failure. As the loading rate increases, there is a corresponding increase in the number of shear cracks, leading to a decrease in the overall ductility and toughness of SFRC. Moreover, since the number of shear cracks notably increases right before SFRC fracture, this can serve as a safety warning of the impending failure. Furthermore, the cumulated AE curve displays a strong discontinuity in the occurrence of an unstable fracturing process in SFRC, which can also be forecasted by the AE time-scaling coefficient β_t. The AE and DIC features can be used as failure precursors in the field of structural surveying, offering an accurate technical support for engineering failure warnings.

Keywords: fibre-reinforced concrete; acoustic emission; digital image correlation; failure precursor; ductile-to-brittle transition

Citation: Jiang, Z.; Zhu, Z.; Accornero, F. Tensile-to-Shear Crack Transition in the Compression Failure of Steel-Fibre-Reinforced Concrete: Insights from Acoustic Emission Monitoring. *Buildings* **2024**, *14*, 2039. https://doi.org/10.3390/buildings14072039

Academic Editor: Mizan Ahmed

Received: 17 June 2024
Revised: 26 June 2024
Accepted: 1 July 2024
Published: 4 July 2024

1. Introduction

Steel-fibre-reinforced concrete (SFRC) is a composite material that can be utilized in civil engineering to enhance the overall performance of structures [1,2]. The incorporation of steel fibres enables concrete to maintain a certain level of strength and deformation capacity after cracking, substantially improving its toughness [3]. The toughening effect is closely linked to the elastic modulus, tensile strength, and interface bonding strength of the steel fibres [4]. Currently, SFRC has broad application prospects in bridge and structural engineering, and the SFRC deck overlay has been rapidly applied in both newly built and existing bridges. However, the in-service SFRC may suffer from damage, posing a risk to the long-term durability of the engineering structures. Therefore, monitoring the damage evolution of in-service concrete has considerable significance for structural safety. Uniaxial compression tests can replicate the stress conditions encountered in engineering scenarios, facilitating the evaluation of SFRC's practical application potential in engineering structures. Given that cracking behaviour in SFRC is difficult to observe directly, acoustic emission (AE) technology provides a non-destructive monitoring method [5,6] useful to detect internal damage evolution [7,8]. AE waves can be measured by sensors placed on structural surfaces, providing crucial information on crack propagation [9–12]. On the

other hand, digital image correlation (DIC) is a non-contact optical measurement method that tracks the motion of points on a surface, by analysing the randomly distributed speckle patterns, facilitating real-time observation of surface displacement and strain [13–16]. In addition, advanced technologies like deep learning for crack detection enhance the accuracy of damage detection and monitoring in concrete structures [17].

Considering the mechanical responses of SFRC under different loading conditions, AE technology offers better insights into the damage mechanisms of SFRC at the microscopic level. In particular, Meng et al. [18] investigated the mechanical properties of concrete reinforced with steel and polypropylene fibres under triaxial cyclic compression, revealing that changes in loading rates alter the crack size, propagation speed, deformation, and failure patterns in the concrete material. Li et al. [19] conducted axial compression tests and AE monitoring on SFRC samples by varying fibre volume fractions, then examining fracture evolution and fractal characteristics. Ren et al. [20] investigated the damage characteristics of SFRC with different steel fibre contents, detecting specific AE signal characteristics for the different post-cracking stages. In [21], the failure of plain concrete samples is found to be dominated by tensile cracks, changing to shear-crack failure by increasing the fibre volume fraction. Xu et al. [22] used waste porcelain as a coarse aggregate in rubber concrete containing steel fibres, investigating compressive strength, microstructure, and the evolution of damage using AE technology. Cai et al. [23] introduced a damage evolution model and examined the damage characteristics using AE. In recent studies, AE and DIC techniques have been used together to evaluate the fracture process, which depends on the characteristic structural size scale [24–26].

Concrete behaviour can be enhanced by adding fibre reinforcements: in this way, the transition from micro- to macro-cracks can be effectively inhibited, as shown in Figure 1, thus leading to a significant improvement in the mechanical properties of the material [27]. Fibres efficiently bridge the micro-cracks generated during loading and restrain the growth of the macro-cracks [28,29], as shown in Figure 2. Ning et al. [30] ascribed the enhancement of SFRC impact resistance to the strengthening effect due to steel fibres when micro-cracks propagate during the impact process. Nguyen et al. [31] investigated the effects of fibres on the tensile strength and the self-sensing capacity of SFRC.

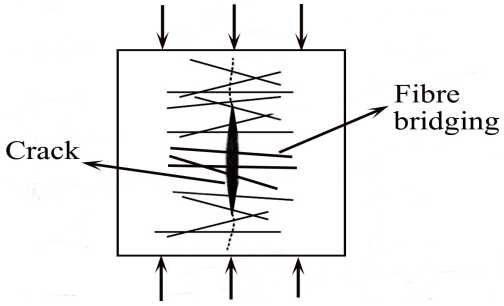

Figure 1. Bridging mechanism of fibre reinforcements.

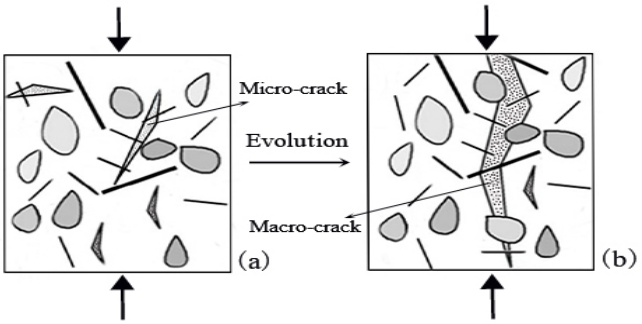

Figure 2. Micro- and macro-cracks bridged by fibres. (**a**) Micro-crack stage; (**b**) Macro-crack stage.

Figure 3 shows a diagram of the meso-scale damage mechanism in SFRC, including matrix cracking, aggregate–matrix cracking, fibre debonding, and fibre slippage. Concrete damage is caused by the propagation of pre-existing internal cracks, which expand primarily along the weak interfaces of aggregate and mortar [32]. After primary crack initiation, the elastic–plastic deformation of fibres, fibre debonding, and fibre slippage become the main damage mechanisms. Fibres with a disordered distribution effectively limit the propagation and coalescence of cracks, causing a change in the direction of cracks, ultimately improving the cracking resistance of concrete.

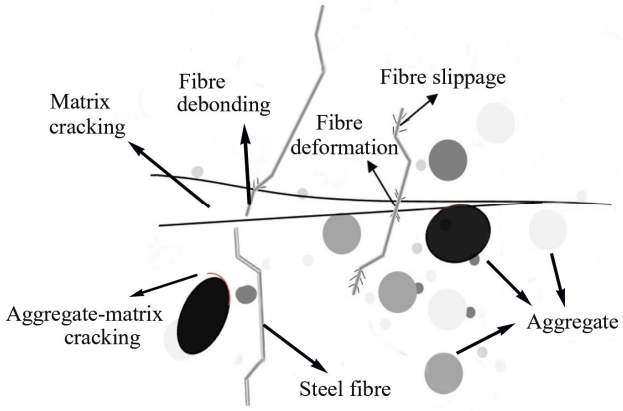

Figure 3. Meso-scale damage of SFRC.

Although several research studies have been conducted on the performance and properties of SFRC, these studies lack rigorous analyses of the failure mechanism responsible for the main variations in AE characteristics. In addition, the crucial role of AE signals, which are effective precursors of SFRC failures, has not yet been clarified. Furthermore, limited attention has been paid to the fracture evolution of SFRC using combined AE and DIC techniques. Therefore, further investigation on the effects of loading rate on damage behaviour of SFRC is necessary, as well as on the role of failure precursor of AE signals in SFRC. This paper conducted AE and DIC monitoring on SFRC samples in uniaxial compression and proposed a new interpretation of the bridging mechanisms of fibre reinforcements in concrete. For all the tests, cumulated AE, *b*-value, β_t coefficient, average frequency, and rise angle are considered to describe the SFRC failure mechanisms. The findings can provide useful insights into the field of engineering failure warning.

2. Experimental Setup

2.1. Sample Preparation

SFRC composited with orthotropic steel decks through shear studs can increase the stiffness of the bridge deck, improve its fatigue performance, and enhance the durability of the pavement layer. Based on the mix ratio of SFRC material used in bridge decks of a new bridge project, a set of SFRC samples in compression are made and tested in this study.

SFRC sample is mainly composed of cement, stone, sand, and randomly distributed short steel fibres, as shown in Figure 4. The concrete grade is C50. SFRC consists of ordinary Portland cement (grade 42.5), river sand with a fineness modulus of 3.0, granite crushed stone of 5–30 mm, and a high-efficiency carboxylate water reducer with a concentration of 10.8%. The mix ratio of cement/sand/stone/water is 1:1.49:2.51:0.32 (Table 1), with a water/cement ratio of 0.32. The normal concrete (NC) sample uses the C50 normal-strength concrete and the same mix ratio, without adding steel fibres. The steel fibres used in SFRC samples are the shear-wave type with a length of 38 mm, an aspect ratio of 60, and a fibre volume fraction of 1%. SFRC mechanical properties are listed in Table 2.

(**a**) (**b**) (**c**) (**d**)

Figure 4. Main components of SFRC: (**a**) Aggregate; (**b**) Sand; (**c**) Cement; and (**d**) Steel fibres.

Table 1. SFRC mix proportion (kg/m^3).

Component	Cement	Sand	Stone	Water	Steel Fibre	Carboxylate Water Reducer
Dosage	480	713	1032	155	75	9.6

Table 2. SFRC mechanical properties.

Material	Compression Strength (MPa)	Elastic Modulus (GPa)	Flexural Strength (MPa)	Splitting Strength (MPa)
SFRC	64.8	39.0	6.8	4.6

Figure 5 shows the prepared SFRC samples, which measure 100 × 100 × 100 mm. During the test preparation, the cement material and aggregate are first dry mixed for 2 min, and then, water is added to achieve a sticky consistency. The steel fibres are evenly poured into a 2 cm screen, and the final mix is obtained by stirring for another 2 min to prevent fibre clustering. The SFRC samples are demoulded 24 h after pouring and placed in a standard curing room for 28 days. After removal, they are dried in a natural environment, exhibiting a compressive strength equal to 64.8 MPa (Table 2). Before testing, matte black paint is applied to the sample surface to create speckle patterns (see Figure 5b), with a speckle size between 5 and 7 pixels.

(**a**) Samples (**b**) Speckles

Figure 5. Overview of test samples.

2.2. Testing System

As shown in Figure 6, a 200 t MATEST actuator eproduced in Jinan, China is employed to conduct uniaxial compression tests on SFRC samples. The AE system utilized in this test is the Italy LUNITEK ÆMISSION® produced in LaSpezia, equipped with piezoelectric sensors (range: 10 kHz–1 MHz). Each AE channel has independent threshold triggers, automatically extracting AE signal parameters for continuous monitoring. One AE sensor is positioned on a vertical side of each SFRC sample, coupled with high-vacuum grease and fixed to the sample with tape as depicted in Figure 6b. The AE waves captured by the sensor undergo a 60 dB amplification before processing, with the acquisition threshold set to 2 mV.

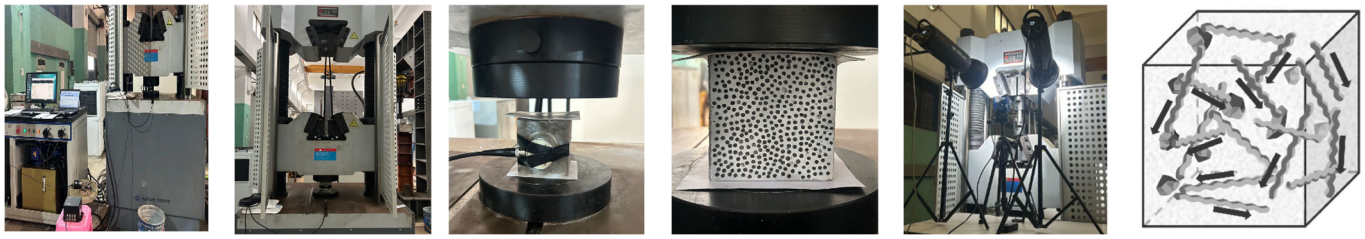

(**a**) Loading system (**b**) Actuator (**c**) AE sensor (**d**) Back speckles (**e**) DIC device (**f**) Fibre arrangement

Figure 6. Test setup.

Additionally, the DIC equipment is simultaneously employed for real-time recording, as shown in Figure 6d. The speckle patterns are analysed through the image analysis system to detect the surface displacement and to calculate the related strain.

The entire loading process adopts displacement-controlled loading, with rates of 0.4 mm/min, 0.8 mm/min, and 1.2 mm/min, respectively (see Figure 7). Both AE and DIC techniques are set on continuous and real-time data acquisition during the fracturing process, allowing the initiation and growth of micro-cracks to be monitored during the whole loading process.

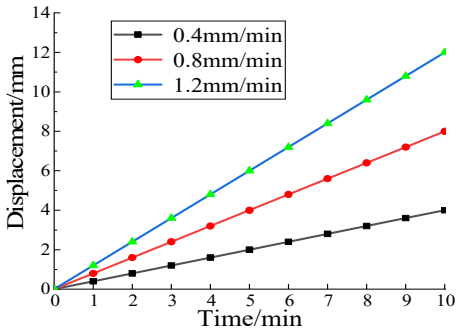

Figure 7. Loading regimes.

2.3. AE Analysis

2.3.1. β_t and *b*-Value

The number N and the total number N_d of AE events recorded up to the end of the monitoring period are expressed as dimensionless functions of time, t, thus defining the evolution of damage as follows [33]:

$$\eta = \frac{N}{N_d} = \left(\frac{t}{t_d}\right)^{\beta_t} \quad (1)$$

where β_t is the time-scaling coefficient that characterizes the time evolution of the damage process. $\beta_t > 1$ reveals unstable crack propagation, whereas $\beta_t < 1$ indicates that the damaging process slows down [33].

On the other hand, *b*-value is obtained by the statistical distribution of the AE signal magnitudes fitted by the GR law [34]:

$$\log_{10}(N_{AE}) = a - bM \quad (2)$$

where A_{max} is the signal peak amplitude, and N_{AE} is the number of AE events with a magnitude greater than M. The *b*-value represents the negative slope of the GR law (Figure 8), which can be fitted by means of the least-squares method. *b*-value usually ranges from 1.5 to 1, revealing the transition from a distribution of micro-cracks in the sample volume (3-D) to a dominant macro-crack (crack surface, 2-D) [35].

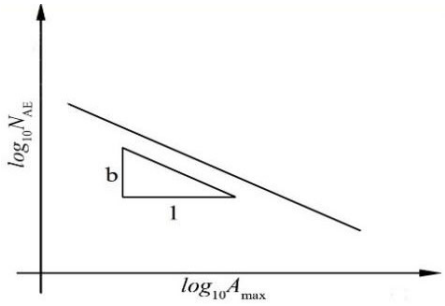

Figure 8. GR's law and AE events.

2.3.2. AF and RA

The main AE characteristic parameters deduced from the acoustic waves are shown in Figure 9a, with some qualitative information about crack classification, such as average frequency (*AF*) and rise angle (*RA*), being obtained. According to JCMS-III B57066 [36], *AF* versus *RA* can be calculated based on the following relationships [37]:

$$AF = \frac{RC(RingingCount)}{DT(\mathrm{DurationTime})} \tag{3}$$

$$RA = \frac{RT(RiseTime)}{A_{\max}(\mathrm{Amplitude})} \tag{4}$$

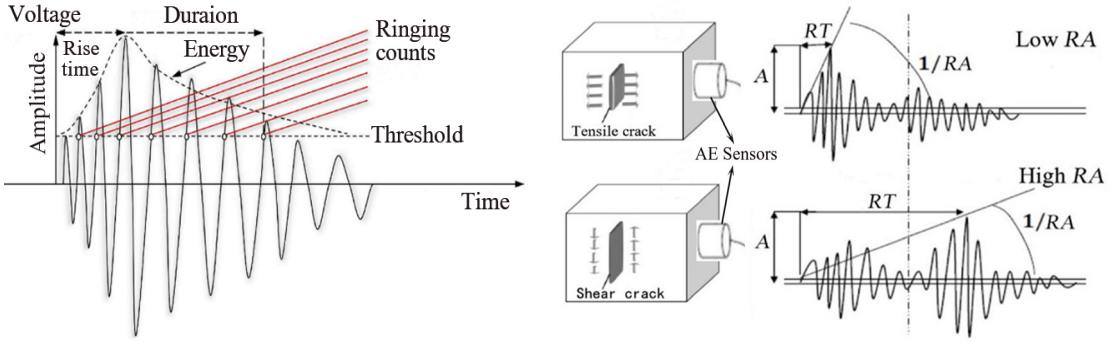

(**a**) Acoustic wave features (**b**) Crack classification

Figure 9. Crack type and AE.

In Equations (3) and (4), *RC* represents the number of signal oscillations greater than the AE threshold, *DT* is the time elapsed between the first and the last signal oscillation above the AE threshold, *RT* is the time between the first signal oscillation crossing the threshold and the maximum signal amplitude, and $A_{\max}$ is the signal peak amplitude. *AF* is measured in kHz, whereas *RA* is measured in ms/V. Following the RILEM Recommendation [38], shear cracks are characterized by relatively low *AF* and high *RA* values, whereas tensile cracks are characterised by higher *AF* and lower *RA* values, as shown in Figure 9. AE signals from tensile cracks exhibit characteristics of high ringing counts, large amplitude, and short rise time. This is because a significant amount of energy is released at tensile crack initiation. In contrast, the AE signals from shear crack emissions have fewer ringing counts, longer rise times, and longer durations [39].

3. Experimental Observations

3.1. Damage Stages and Thresholds

Concrete fracture is a multi-scale phenomenon that begins with the initiation and propagation of micro-cracks and continues with the development and propagation of macro-cracks, eventually resulting in a catastrophic failure depending on the structural brittleness. Although the AE data obtained at various loading rates exhibit some differences, they consistently indicate patterns in line with the different damage stages. Thus, the load–displacement curve of SFRC (Figure 10) can be divided into three distinct stages, characterised by the first cracking load (F_{fc}) and the ultimate load (F_{max}). Additionally, the critical load in stage III (F_{cr}) is also highlighted in Figure 10.

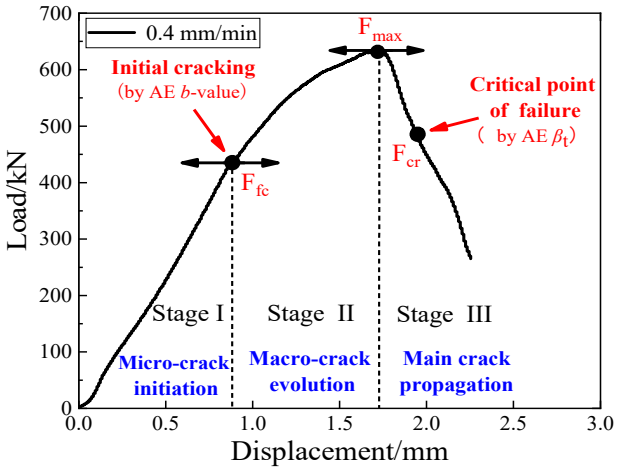

Figure 10. Load–displacement curve with indicated three stages.

Stage I involves the micro-crack initiation (see Figure 2a). As the external load increases, the elastic stage takes place, characterized by a linear increase in the load–displacement curve. The matrix predominantly bears the external load, and the fibres do not play a significant role. The source of AE signals is attributed to a complex mechanism, including matrix cracking and aggregate-to-matrix cracking (see Figure 3).

Stage II entails the macro-crack evolution (see Figure 2b). After reaching the macro-crack initiation point, that is, the first cracking load (F_{fc}), the micro-cracks transform into localized macro-cracks, for which fibres significantly restrict the growth, as shown in Figure 1. Then, the slope of the load–displacement curve continues to decrease, displaying an upward convex growth until reaching the ultimate load (F_{max}). Meanwhile, the primary source of AE signals is attributed to the fibre debonding and deformation (see Figure 3).

Stage III involves the main crack propagation. After the peak load, the SFRC sample presents considerable ductility thanks to the softening branch envisaged by the fibre slippage into the concrete matrix [40]. The slope of the load–displacement curve presents a relatively rapid decline until reaching the critical load (F_{cr}), then culminating in the final failure. Throughout this stage, the AE signals primarily originate from fibre slippage or pull-out (see Figure 3).

3.2. Compressive Toughness Index (CTI)

In uniaxial compression testing, the first cracking load (F_{fc}) and the ultimate load (F_{max}) of SFRC samples hold significant importance. The approach outlined by Khan and Qin [41–43] and Carpinteri et al. [44,45] enables a quantitative depiction of the bearing capacity of SFRC. This method defines the areas enclosed by the load–displacement curve as the released energy equal to the summation of dissipated and emitted ones and equivalent to the integral of the curve. By drawing parallel lines to the Y-axis through points (F_{fc} and F_{max}), the enclosed area is partitioned into three segments: energy released by cracks before initial cracking (A1), energy released from initial cracking to peak (A2), and energy

released until failure (A3), as illustrated in Figure 11. The sum of A1 and A2 yields A4, representing the released energy preceding the ultimate load. In Table 3, A1 and A2 vary during the pre-peak stage of each sample, with A2 gradually diminishing as the loading rate increases, whereas A1 concurrently rises. Elevated loading rates increase the energy dissipation for crack propagation, consequently augmenting A1.

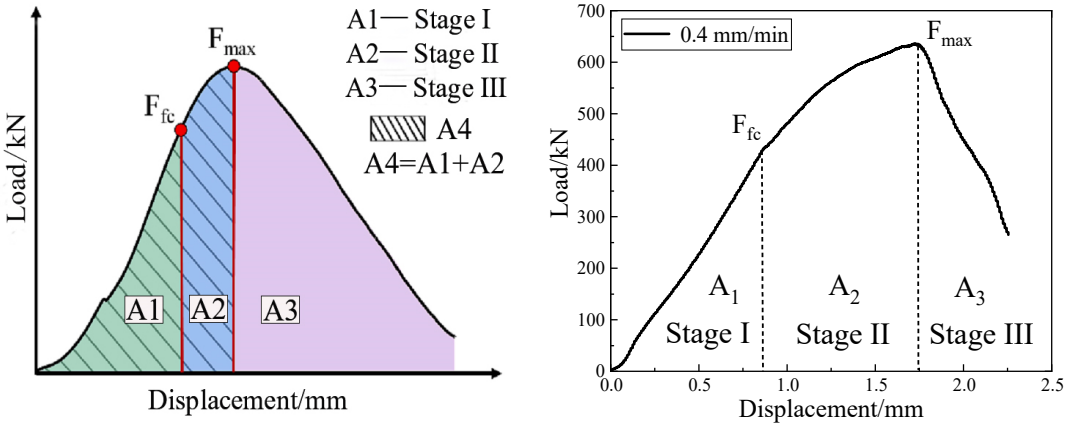

(**a**) Energy release (**b**) SFRC with loading rate 0.4 mm/min

Figure 11. SFRC compressive toughness.

Table 3. Compressive Toughness Index (CTI).

Loading Rate	A1/(kN·mm)	A2/(kN·mm)	A4/(kN·mm)	CTI (A4/A1)
0.4 mm/min	173	492	665	3.84
0.8 mm/min	210	490	700	3.33
1.2 mm/min	275	489	764	2.77

Moreover, the Compressive Toughness Index (CTI), representing the ratio of A4 to A1, indicates the crack resistance of SFRC, offering a quantification of the toughening effect exerted by steel fibres in concrete [46]. Under uniaxial compression, steel fibres constrain the transverse deformation of SFRC samples through bridging action, thereby enhancing SFRC toughness [47]. Table 3 shows that, at loading rates of 0.4 mm/min, 0.8 mm/min, and 1.2 mm/min, the SFRC CTI is 3.84, 3.33, and 2.77, respectively. This suggests that the energy required for cracking increases as the loading rate decreases. The loading rate significantly influences the toughness of SFRC. At a low loading rate, steel fibres effectively diminish brittle cracking and enhance overall integrity and ductility, whereas higher rates may entail brittle fractures.

3.3. DIC Monitoring

In Figure 12, the SFRC damage process is represented throughout various stages. Initially, the surface of the SFRC samples exhibits no cracks (Figure 12a), and as the loading increases, micro-cracks emerge gradually and spread within the sample volume. As the macro-cracks initiate (Figure 12b), the deformation of samples becomes increasingly governed by the fibre-bridging action. During this stage, there is a rattling sound of fibres detaching from the concrete matrix. The surface of the samples is slightly bulging outwards, and there are only a few debris falling. In the final failure (Figure 12c,d), the sample retains its integrity, and the fibre-bridging effect inhibits the main crack propagation, transforming the SFRC samples from a brittle fracture to a relatively ductile failure mode.

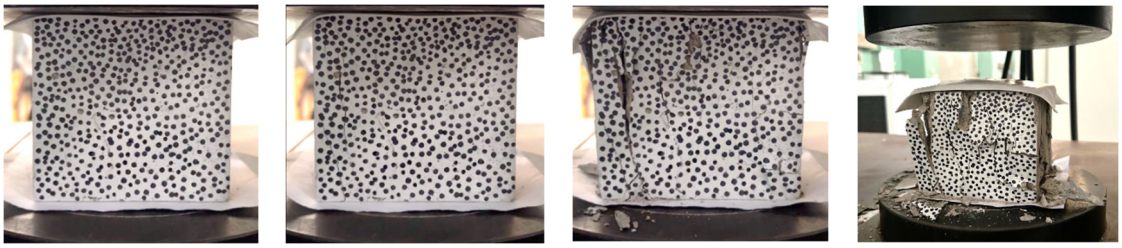

(**a**) Initial loading (**b**) Initial cracking (**c**) Fracture (**d**) Failure

Figure 12. SFRC damage evolution (loading rate: 0.4 mm/min).

Figures 13 and 14 present the results of the DIC strain analysis. A comparison between SFRC and NC in Figure 13c,d and Figure 14c,d reveals that the SFRC samples exhibit multiple dense and slender cracks, whereas NC samples during the damage process show a single vertical crack with a larger width (Figures 14d and 15b). Results of SFRC at different loading rates in Figures 13a–c and 14a–c show that, under low loading rates, the main cracks in the SFRC samples are tensile types. The observed number of surface cracks is relatively small, and samples have slight transverse deformation, with no evident fragment detachment from the surface layer, as depicted in Figures 13a and 14a. Conversely, under high loading rates, the number of surface cracks in the SFRC samples increases. The main cracks are both tensile and shear types, accompanied by local fragment detachment at the edges, with severe transverse deformation of samples, as illustrated in Figures 13c and 14c. In addition, some new inclined shear cracks appear with the evolution of the damage process.

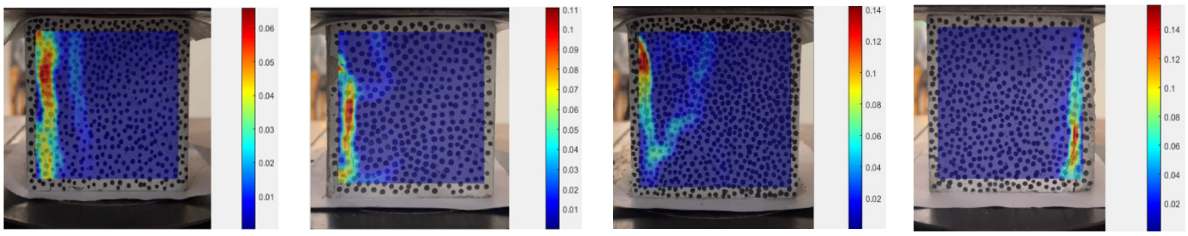

(**a**) SFRC—0.4 mm/min (**b**) SFRC—0.8 mm/min (**c**) SFRC—1.2 mm/min (**d**) NC—1.2 mm/min

Figure 13. DIC strain analysis at initial cracking with different loading rates.

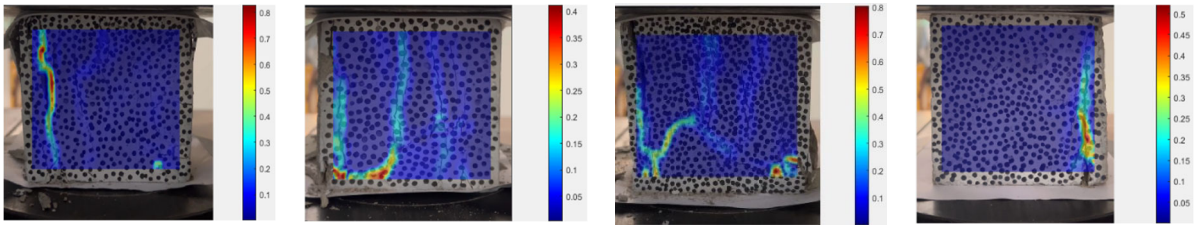

(**a**) SFRC—0.4 mm/min (**b**) SFRC—0.8 mm/min (**c**) SFRC 1.2 mm/min (**d**) NC—1.2 mm/min

Figure 14. DIC strain analysis at fracturing with different loading rates.

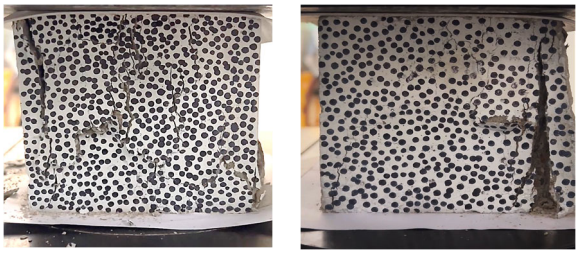

(**a**) SFRC 1.2 mm/min (**b**) NC—1.2 mm/min

Figure 15. Comparison of SFRC and NC sample failures.

4. AE Monitoring Results

4.1. β_t and b-Values

The AE events are fitted into groups of 100 events to obtain β_t and *b*-value. Figure 16a–c depicts the evolution of β_t and *b*-value in SFRC samples, and dashed lines represent the regression curve of *b*-values, and the average *b*-value decreases as the loading rate increases. It can be observed that, at high loading rates, the regression curve of *b*-values shows a decreasing trend, indicating unstable crack propagation. Conversely, at low loading rates, samples exhibit relatively stable crack propagation, with an almost constant *b*-value.

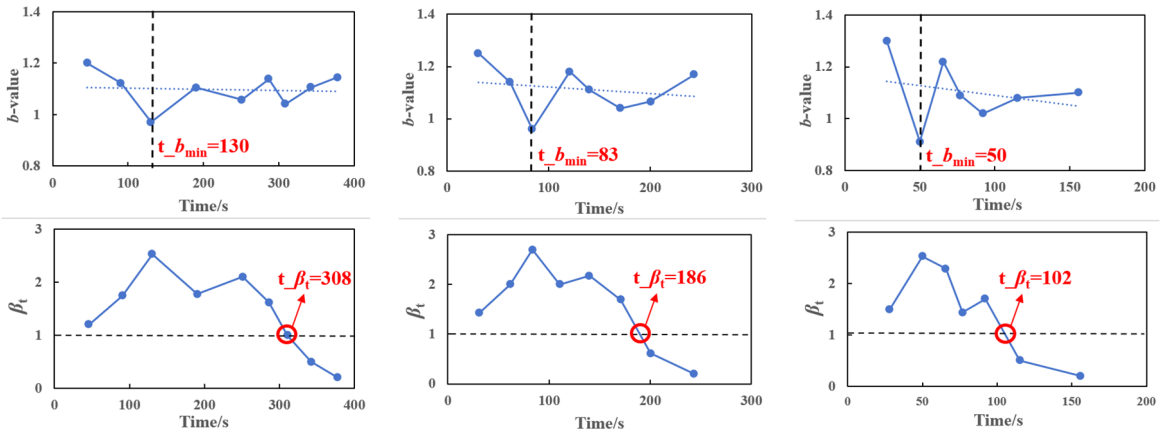

(**a**) SFRC—0.4 mm/min (**b**) SFRC—0.8 mm/min (**c**) SFRC—1.2 mm/min

Figure 16. β_t and *b*-values at different loading rates.

During the initial loading stage, there are fluctuations in the *b*-value, exhibiting a pattern of initial decrease followed by an increase, consistent with the damage behaviour of concrete. The point at which the *b*-value reaches its minimum corresponds to the transition from micro- to macro-cracks, denoted as t_b_{min}, as illustrated in Figure 16a–c.

Specifically, at a rate of 0.4 mm/min (see Figure 16a), the SFRC sample reaches t_b_{min} at 130 s, with b_{min} = 0.9 and β_t = 2.5 ($\beta_t > 1$), representing the coalescence of micro-cracks (indicated by the dashed line in Figure 16a). Similarly, at a rate of 0.8 mm/min (Figure 16b), we have $b_{min} \approx 1.0$ at 83 s, with β_t = 2.7 ($\beta_t > 1$), whereas under a loading rate of 1.2 mm/min (Figure 16c), we have b_{min} = 0.9 at 50 s, with β_t = 2.6 ($\beta_t > 1$). It is evident that t_b_{min} reveals an unstable damage condition with numerous micro-crack coalescence in a main fracture surface, forming several macro-cracks on the SFRC sample surfaces.

The β_t curves depicted in Figure 16a–c exhibit a decreasing trend. The critical points are marked as t_β_t (see Figure 16). In addition, as illustrated in Figure 17, the critical time obtained from the β_t coefficient corresponds to the occurrence of the unstable fracturing process, with all the micro-cracks organizing on the main fracture surface. These findings confirm that in the AE time series preceding the critical point t_β_t, β_t >1 indicate unstable

crack propagation, whereas, after reaching the critical point t_β_t, β_t <1, the main energy dissipation occurs.

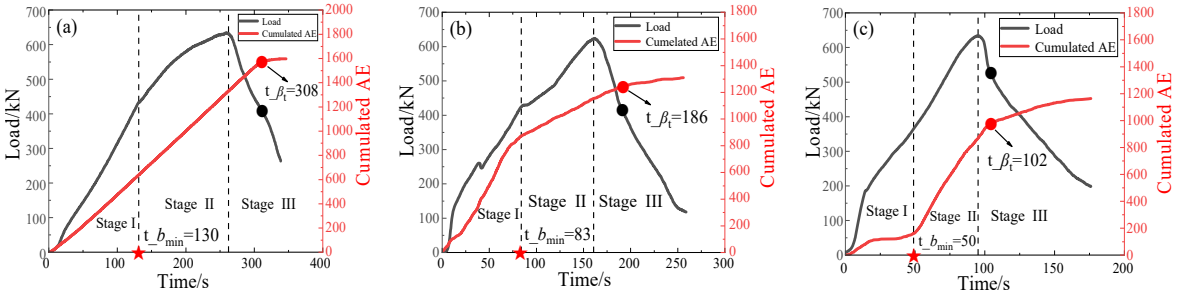

Figure 17. Cumulated AE and loading history at loading rates of (**a**) 0.4 mm/min, (**b**) 0.8 mm/min, and (**c**) 1.2 mm/min.

4.2. Cumulated AE and Loading History

Figure 17 shows the cumulated AE and the loading history under different loading rates. Additionally, t_β_t and t_b_{min}, determined by β_t and *b*-values, are also highlighted in Figure 17.

In stage I, the cumulated AE curve grows linearly. In stage II, when the concrete matrix initially cracks, the steel fibres bridge the crack faces in the concrete. As the load increases, extensive cracking occurs in the samples around the peak load. In stage III, the samples suffer severe damage, and the load-bearing capacity tends to decrease. The cumulated AE in this stage decreases, and eventually, no AE signals appear, indicating a decay period.

At a low loading rate, there is an increase in the total number of AE events (Figure 17a), signifying the initiation of numerous micro-cracks in the SFRC. Conversely, as the loading rate increases, SFRC indicates relatively more brittle behaviour, leading to sudden cracking and increased AE events, thereby indicating that the SFRC forms cracks with a larger width (Figure 17b,c).

The t_β_t determines the occurrence of an unstable fracturing process, marked by a significant inflection point in the cumulated AE, signalling a decrease in AE event growth. It is evident that, by increasing the loading rate, the post-peak softening branch becomes steeper, indicating a transition from ductile to relatively brittle behaviours (Figure 17c).

4.3. Crack Mechanisms Analysed by AF and RA

The classification of cracks in concrete materials holds significant importance in predicting the types of damage under diverse loading conditions. The damage process, as defined in the previous sections (Figures 10 and 17), can be analysed by *AF* and *RA* (Figures 18 and 19).

As depicted in Figure 19, the proportions of shear cracks in SFRC present a consistent change in each stage by considering different loading rates: a gradual transition from tensile cracks to shear cracks can be detected. In stage I, the nascent cracks are mainly tensile. For instance, at a loading rate of 0.4 mm/min, the ratio of tensile cracks to shear cracks is approximately 7:3, corresponding to the cracking of aggregate and matrix. In stage II, a significant number of new cracks emerge. The most noticeable change occurs in the proportion shift from tensile to shear cracks, and the number of shear and tensile cracks becomes roughly equal, with a ratio close to 1:1. In stage III, shear cracks begin to dominate, and the ratio of tensile cracks to shear cracks is approximately 1:2. Here, shear cracks represent 68%, 74%, and 82% of the total damage, at loading rates of 0.4, 0.8, and 1.2 mm/min, respectively. The analysis indicates that, by increasing the loading rate, the proportion of shear cracks increases, confirming that the high loading rate reduces the overall ductility of SFRC samples.

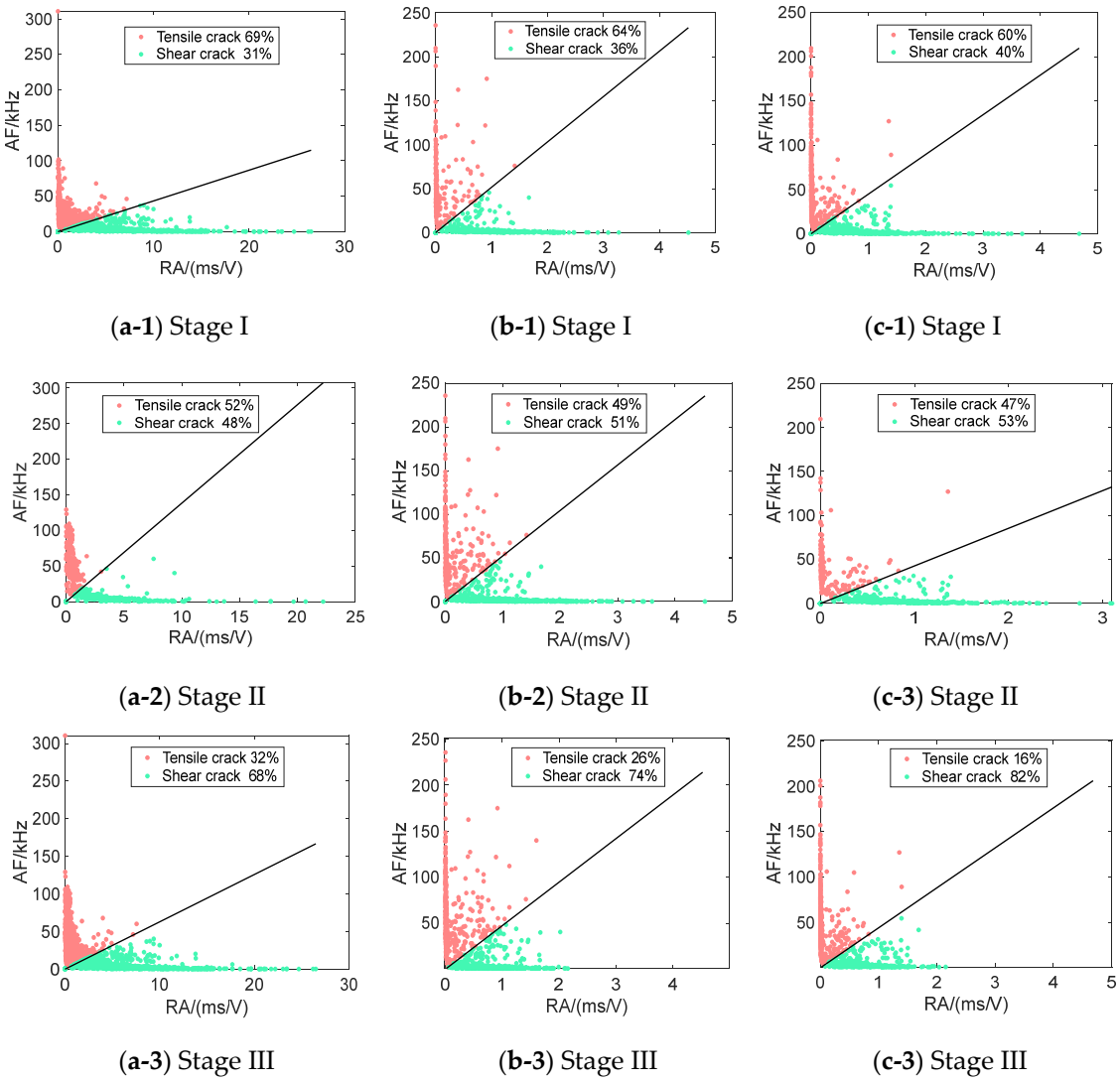

Figure 18. *AF* and *RA* in SFRC samples: (**a-1**–**a-3**) 0.4 mm/min, (**b-1**–**b-3**) 0.8 mm/min, and (**c-1**–**c-3**) 1.2 mm/min.

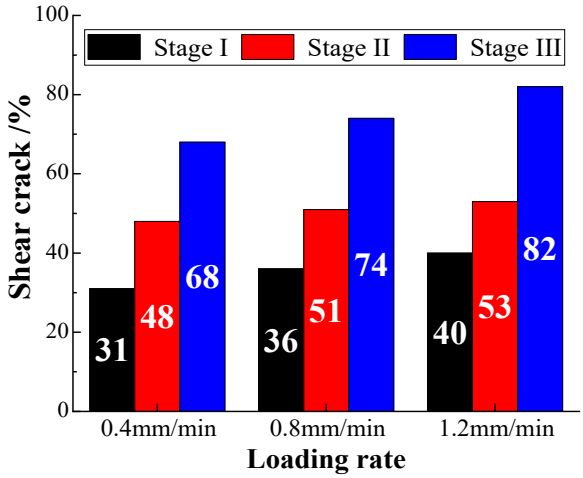

Figure 19. Shear cracks in each damage stage and at different loading rates.

5. Failure Mechanisms

The combined AE and DIC results can explain the final failure mechanisms of the SFRC samples.

As depicted in Figure 20, during the early stage I, the initial damage primarily results from tensile fracture, indicating the onset of matrix cracking. At this stage, fibre reinforcements are not engaged in reinforcing the matrix (Figure 20a). In the following stage II, with the increase in crack propagation, the fibres provide their action to bridge the tensile cracks (Figure 20b). At the same time, the quantity of shear cracks begins to increase. In the final stage III, as the shear stiffness of the fibres is relatively small, with the further increase in the load, the matrix fractures along the shear plane; thus, the quantity of shear cracks begins to dominate (Figure 20c).

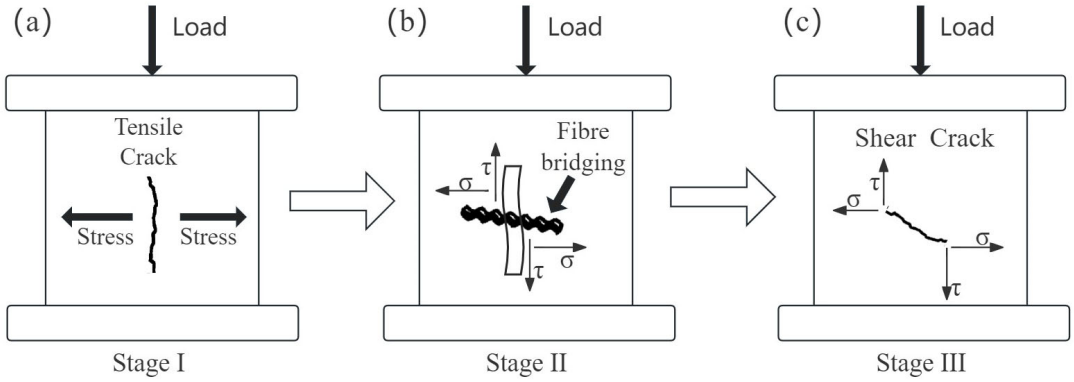

Figure 20. Tensile-to-shear crack transition. (**a**) Stage I; (**b**) Stage II; (**c**) Stage III.

Therefore, at different loading rates, the cracks in the whole process gradually change from the tensile to the shear mode (Figure 21), the latter being the main cause of the SFRC failure, as also evidenced by the DIC results. The tensile-to-shear crack transition is essential for the SFRC failure precursor under different loading conditions.

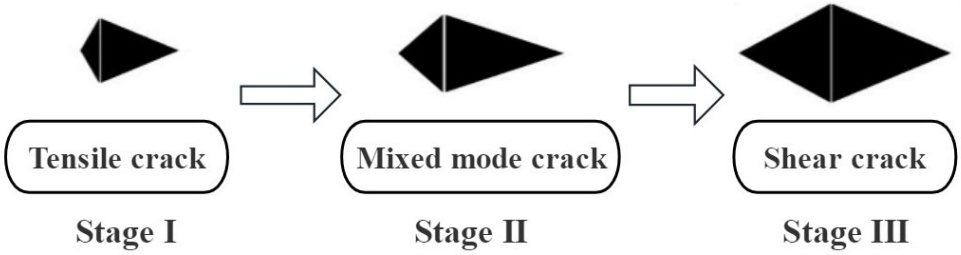

Figure 21. Variation in waveforms and crack modes during the fracturing process.

The incorporation of fibres significantly enhances the toughness and ductility of SFRC compared to NC. This improvement can be attributed to the bridging effect of the fibres, which effectively delay the transition from micro-cracks to macro-cracks, thus providing additional energy absorption capacity [1,2,48]. The evidences offered by the tensile-to-shear crack transition observed in SFRC represent critical aspect of the material failure mechanism. This transition is driven by the load redistribution facilitated by the action of the fibres, which enhances the concrete ability to withstand higher loads before failing.

The use of AE monitoring in this study provides reliable precursors for predicting the imminent failure of SFRC. Parameters such as the cumulated AE curve and the AE time-scaling coefficient β_t are effective in forecasting the unstable fracturing processes. The consistent results coming from the application of these AE tools, also considering different loading rates, further validates their reliability as early warning indicators. The loading rate has a substantial impact on the number of shear cracks, and consequently on the ductility and toughness of SFRC. Higher loading rates lead to an increase in the

number of shear cracks and reduced the ductility (brittle failure mode). Conversely, lower loading rates result in dominant tensile cracks and large energy absorption, leading to enhanced ductility and toughness. While this study focuses on SFRC, the underlying principles of fibre-reinforcement mechanical behaviour, such as crack bridging and energy dissipation, are applicable to other types of fibre-reinforced brittle-matrix composites [49] and structural schemes.

6. Conclusions

The present study investigates the AE and DIC features during damage in SFRC samples under different loading rates. The following conclusions can be outlined as follows:

(1) In the early fracturing stage, fibres did not exert their toughening effects, with the AE signals originating from the matrix and aggregate–matrix interface cracking. In the intermediate stage, as macro-cracks extend, fibres begin to restrain the crack propagation, whereas AE arises from the fibre debonding. In the final stage, the fibre bridging action prevents large-scale fracture surfaces, with AE originating from fibre slippage or pull-out.

(2) The Compressive Toughness Index serves as a damage parameter to assess the impact of fibres on the toughness of the concrete matrix. The toughness of SFRC is influenced by the loading rate, where high loading rates lead to relatively brittle fracturing, whereas low loading rates allow the samples to release energy in a more ductile way.

(3) DIC monitoring reveals that SFRC exhibits better integrity compared to NC when damaged, shifting from brittle to ductile behaviour. SFRC cracks display dense and slender morphology, whereas NC presents a single vertical crack with a larger width. As the loading rate increases, the dominant cracks in SFRC shift from tensile to shear, accompanied by large transverse deformations.

(4) AE *b*-value can determine the exact time of initial cracking in SFRC, whereas β_t can determine the occurrence of unstable fracturing process. As the loading rate increases, the regression curve of the *b*-value shows a downward trend, revealing unstable crack propagation.

(5) The fibre bridging action facilitates the shift from tensile to shear cracks, thus becoming the main cause of SFRC failure. *AF* and *RA* analysis describes a progressive tensile-to-shear crack transition. Since the quantity of shear cracks significantly increases before SFRC failure, this can serve as a safety warning. As the loading rate increases, there is a corresponding increase in the quantity of shear cracks, leading to a decrease in the overall ductility and toughness of SFRC.

Author Contributions: Z.J.: writing—original draft, methodology, investigation, data curation, and conceptualization. Z.Z.: writing—review and editing, writing—original draft, methodology, investigation, data curation, and conceptualization. F.A.: methodology, supervision, and conceptualization, writing—review and editing. All authors have read and agreed to the published version of the manuscript.

Funding: This research was funded by National Natural Science Foundation of China (52278509) and Natural Science Foundation of Guangdong Province (2022A1515 010261) (Zhiwen Zhu), and STU Outstanding Talent Grant N. 140-09423016 (Federico Accornero).

Data Availability Statement: The raw data supporting the conclusions of this article will be made available by the authors on request.

Conflicts of Interest: The authors declare that they have no known competing financial interests or personal relationships that could have appeared to influence the work reported in this paper.

References

1. Accornero, F.; Rubino, A.; Carpinteri, A. Post-cracking regimes in the flexural behaviour of fibre-reinforced concrete beams. *Int. J. Solids Struct.* **2022**, *248*, 111637. [CrossRef]
2. Accornero, F.; Rubino, A.; Carpinteri, A. Ultra-low cycle fatigue (ULCF) in fibre-reinforced concrete beams. *Theor. Appl. Fract. Mech.* **2022**, *120*, 103392. [CrossRef]

3. Zhou, M.; He, X.; Wang, H.; Wu, C.; He, J. Mesoscale modeling of polypropylene fiber reinforced concrete under split tension using discrete element method. *Constr. Build. Mater.* **2023**, *404*, 133274. [CrossRef]
4. Yoo, D.-Y.; Kim, J.-J.; Park, J.-J. Effect of fiber spacing on dynamic pullout behavior of multiple straight steel fibers in ultra-high-performance concrete. *Constr. Build. Mater.* **2019**, *210*, 461–472. [CrossRef]
5. Zheng, Q.; Li, C.; He, B.; Jiang, Z. Revealing the effect of silica fume on the flexural behavior of ultra-high-performance fiber-reinforced concrete by acoustic emission technique. *Cem. Concr. Compos.* **2022**, *131*, 104563. [CrossRef]
6. Han, Q.; Yang, G.; Xu, J.; Fu, Z.; Lacidogna, G.; Carpinteri, A. Acoustic emission data analyses based on crumb rubber concrete beam bending tests. *Eng. Fract. Mech.* **2019**, *210*, 189–202. [CrossRef]
7. Lacidogna, G.; Piana, G.; Accornero, F.; Carpinteri, A. Multi-technique damage monitoring of concrete beams: Acoustic Emission, Digital Image Correlation, Dynamic Identification. *Constr. Build. Mater.* **2020**, *242*, 118114. [CrossRef]
8. Li, W.; Jiang, Z.; Yu, Q. Multiple damaging and self-healing properties of cement paste incorporating microcapsules. *Constr. Build. Mater.* **2020**, *255*, 119302. [CrossRef]
9. Carpinteri, A.; Lacidogna, G.; Accornero, F. Fluctuations of $1/f$ Noise in Damaging Structures Analyzed by Acoustic Emission. *Appl. Sci.* **2018**, *8*, 1685. [CrossRef]
10. Aggelis, D.G. Classification of cracking mode in concrete by acoustic emission parameters. *Mech. Res. Commun.* **2011**, *38*, 153–157. [CrossRef]
11. Aggelis, D.; Mpalaskas, A.; Matikas, T. Investigation of different fracture modes in cement-based materials by acoustic emission. *Cem. Concr. Res.* **2013**, *48*, 1–8. [CrossRef]
12. Rasheed, M.A.; Prakash, S.S.; Raju, G.; Kawasaki, Y. Fracture studies on synthetic fiber reinforced cellular concrete using acoustic emission technique. *Constr. Build. Mater.* **2018**, *169*, 100–112. [CrossRef]
13. Golewski, G.L. Measurement of fracture mechanics parameters of concrete containing fly ash thanks to use of Digital Image Correlation (DIC) method. *Measurement* **2019**, *135*, 96–105. [CrossRef]
14. Huang, Z.; Tu, Y.; Meng, S.; Sabau, C.; Popescu, C.; Sas, G. Experimental study on shear deformation of reinforced concrete beams using digital image correlation. *Eng. Struct.* **2018**, *181*, 670–698. [CrossRef]
15. Bello, I.; González-Fonteboa, B.; Wardeh, G.; Martínez-Abella, F. Characterization of concrete behavior under cyclic loading using 2D digital image correlation. *J. Build. Eng.* **2023**, *78*, 107709. [CrossRef]
16. Liu, J.; Kanwal, H.; Tang, C.; Hao, W. Study on flexural properties of 3D printed lattice-reinforced concrete structures using acoustic emission and digital image correlation. *Constr. Build. Mater.* **2022**, *333*, 127418. [CrossRef]
17. Andrushia, A.D.; Lubloy, E. Deep learning based thermal crack detection on structural concrete exposed to elevated temperature. *Adv. Struct. Eng.* **2021**, *24*, 1896–1909. [CrossRef]
18. Meng, K.; Xu, L.; Chi, Y. Experimental investigation on the mechanical behavior of hybrid steel-polypropylene fiber reinforced concrete under conventional triaxial cyclic compression. *Constr. Build. Mater.* **2021**, *291*, 123262. [CrossRef]
19. Li, H.; Li, X.; Fu, J.; Zhu, N.; Chen, D.; Wang, Y.; Ding, S. Experimental study on compressive behavior and failure characteristics of imitation steel fiber concrete under uniaxial load. *Constr. Build. Mater.* **2023**, *399*, 132599. [CrossRef]
20. Ren, H.; Li, T.; Ning, J.; Song, S. Analysis of damage characteristics of steel fiber-reinforced concrete based on acoustic emission. *Eng. Fail. Anal.* **2023**, *148*, 107166. [CrossRef]
21. Li, B.; Xu, L.; Shi, Y.; Chi, Y.; Liu, Q.; Li, C. Effects of fiber type, volume fraction and aspect ratio on the flexural and acoustic emission behaviors of steel fiber reinforced concrete. *Constr. Build. Mater.* **2018**, *181*, 474–486. [CrossRef]
22. Xu, J.; Houndehou, J.D.; Wang, Z.; Ma, Q. Experimental investigation on the mechanical properties and damage evolution of steel-fiber-reinforced crumb rubber concrete with porcelain tile waste. *Constr. Build. Mater.* **2023**, *370*, 130643. [CrossRef]
23. Cai, B.; Li, K.; Fu, F. Flexural behavior of steel fiber-reinforced coal gangue aggregate concrete beams. *Structures* **2023**, *52*, 131–145. [CrossRef]
24. Boniface, A.; Saliba, J.; Sbartaï, Z.M.; Ranaivomanana, N.; Balayssac, J.P. Evaluation of the acoustic emission 3D localisation accuracy for the mechanical damage monitoring in concrete. *Eng. Fract. Mech.* **2020**, *223*, 106742. [CrossRef]
25. Zhou, W.; Lv, Z.H.; Li, Z.Y.; Song, X. Acoustic emission response and micro-deformation behavior for compressive buckling failure of multi-delaminated composites. *J. Strain Anal. Eng. Des.* **2016**, *51*, 397–407. [CrossRef]
26. Alam, S.; Loukili, A.; Grondin, F.; Rozière, E. Use of the digital image correlation and acoustic emission technique to study the effect of structural size on cracking of reinforced concrete. *Eng. Fract. Mech.* **2015**, *143*, 17–31. [CrossRef]
27. Zhang, P.; Wang, C.; Gao, Z.; Wang, F. A review on fracture properties of steel fiber reinforced concrete. *J. Build. Eng.* **2023**, *67*, 105975. [CrossRef]
28. Cui, K.; Xu, L.; Tao, T.; Huang, L.; Li, J.; Hong, J.; Li, H.; Chi, Y. Mechanical behavior of multiscale hybrid fiber reinforced recycled aggregate concrete subject to uniaxial compression. *J. Build. Eng.* **2023**, *71*, 106504. [CrossRef]
29. Rooholamini, H.; Hassani, A.; Aliha, M. Fracture properties of hybrid fibre-reinforced roller-compacted concrete in mode I with consideration of possible kinked crack. *Constr. Build. Mater.* **2018**, *187*, 248–256. [CrossRef]
30. Li, N.; Jin, Z.; Long, G.; Chen, L.; Fu, Q.; Yu, Y.; Zhang, X.; Xiong, C. Impact resistance of steel fiber-reinforced self-compacting concrete (SCC) at high strain rates. *J. Build. Eng.* **2021**, *38*, 102212. [CrossRef]
31. Nguyen, D.-L.; Lam, M.N.-T.; Kim, D.-J.; Song, J. Direct tensile self-sensing and fracture energy of steel-fiber-reinforced concretes. *Compos. B Eng.* **2020**, *183*, 107714. [CrossRef]

32. Yin, Y.; Ren, Q.; Shen, L. Study on the effect of aggregate distribution on mechanical properties and damage cracks of concrete based on multifractal theory. *Constr. Build. Mater.* **2020**, *262*, 120086. [CrossRef]
33. Lacidogna, G.; Manuello, A.; Niccolini, G.; Accornero, F.; Carpinteri, A. Acoustic emission wireless monitoring of structures. In *Acoustic Emission and Related Non-Destructive Evaluation Techniques in the Fracture Mechanics of Concrete*; Woodhead Publishing: Cambridge, UK, 2015; pp. 15–40.
34. Colombo, I.S.; Main, I.G.; Forde, M.C. Assessing damage of reinforced concrete beam using "*b*-value" analysis of acoustic emission signals. *J. Mater. Civ. Eng.* **2003**, *15*, 280–286. [CrossRef]
35. Carpinteri, A.; Xu, J.; Lacidogna, G.; Manuello, A. Reliable onset time determination and source location of acoustic emissions in concrete structures. *Cem. Concr. Compos.* **2012**, *34*, 529–537. [CrossRef]
36. *JCMS-III B5706*; Monitoring Method for Active Cracks in Concrete by Acoustic Emission. Federation of Construction Materials Industries: Tokyo, Japan, 2003.
37. Ohtsu, M. Recommendation of RILEM TC 212-ACD: Acoustic emission and related nde techniques for crack detection and damage evaluation in concrete: Test method for classification of active cracks in concrete by acoustic emission. *Mater. Struct.* **2010**, *43*, 1187–1189. [CrossRef]
38. Noorsuhada, M. An overview on fatigue damage assessment of reinforced concrete structures with the aid of acoustic emission technique. *Constr. Build. Mater.* **2016**, *112*, 424–439. [CrossRef]
39. Xu, J.; Niu, X.; Ma, Q.; Han, Q. Mechanical properties and damage analysis of rubber cement mortar mixed with ceramic waste aggregate based on acoustic emission monitoring technology. *Constr. Build. Mater.* **2021**, *309*, 125084. [CrossRef]
40. Mousavinejad, S.H.G.; Gashti, M.F. Effects of alkaline solution to binder ratio on fracture parameters of steel fiber reinforced heavyweight geopolymer concrete. *Theor. Appl. Fract. Mech.* **2021**, *113*, 102967. [CrossRef]
41. Khan, M.; Ali, M. Use of glass and nylon fibers in concrete for controlling early age micro cracking in bridge decks. *Constr. Build. Mater.* **2016**, *125*, 800–808. [CrossRef]
42. Khan, M.; Ali, M. Effectiveness of hair and wave polypropylene fibers for concrete roads. *Constr. Build. Mater.* **2018**, *166*, 581–591. [CrossRef]
43. Qin, Y.; Zhang, X.; Chai, J.; Xu, Z.; Li, S. Experimental study of compressive behavior of polypropylene-fiber-reinforced and polypropylene-fiber-fabric-reinforced concrete. *Constr. Build. Mater.* **2019**, *194*, 216–225. [CrossRef]
44. Carpinteri, A.; Accornero, F. Multiple snap-back instabilities in progressive microcracking coalescence. *Eng. Fract. Mech.* **2018**, *187*, 272–281. [CrossRef]
45. Lacidogna, G.; Accornero, F.; Carpinteri, A. Influence of snap-back instabilities on Acoustic Emission damage monitoring. *Eng. Fract. Mech.* **2019**, *210*, 3–12. [CrossRef]
46. Jang, S.-J.; Yun, H.-D. Combined effects of steel fiber and coarse aggregate size on the compressive and flexural toughness of high-strength concrete. *Compos. Struct.* **2018**, *185*, 203–211. [CrossRef]
47. Ran, J.; Li, T.; Chen, D.; Shang, L.; Li, W.; Zhu, Q. Mechanical properties of concrete reinforced with corrugated steel fiber under uniaxial compression and tension. *Structures* **2021**, *34*, 1890–1902. [CrossRef]
48. Carpinteri, A.; Accornero, F. Residual crack opening in fibre-reinforced structural elements subjected to cyclic loading. *Strength. Fract. Comp.* **2020**, *12*, 63–74. [CrossRef]
49. Carpinteri, A.; Accornero, F.; Rubino, A. Scale effects in the post-cracking behaviour of fibre-reinforced concrete beams. *Int. J. Fract.* **2023**, *240*, 1–16. [CrossRef]